PROJECT ACRONYM: **C3HARME**

PROJECT TITLE: **Next generation ceramic composites for combustion harsh environments and space**

Deliverable 2.5

Atomistic modelling of processes at materials interfaces

TOPIC			H2020-NMP-19-2015-RIA
GA			685594
COORDINATING PERSON			**Yanhui Zhang** yzhang1@tcd.ie
NATURE	Report (R)	DISSEMINATION LEVEL	PU
DUE DATE	[31/05/2018]	ACTUAL DELIVERED DATE	11/05/2018
AUTHORS			Yanhui Zhang, Stefano Sanvito

Table of Revisions

REVISION NUMBER	DATE	WORK PERFORMED	CONTRIBUTORS
1	[09/05/2018]	Production of the document	Yanhui Zhang
2	[30/05/20018]	Technical Revision	Stefano Sanvito
3	[31/05/20018]	Revision and acceptance	D. Sciti

Table of Contents

List of Tables and Figures

Figure 15: Front and top view of heterostructures of (a) $I_{Zr}AA$; (b) $I_{Zr}AB$; (c) I_BAA; (d) I_BAB; (e) $II_{Zr}AA$; (f) $II_{Zr}AB$; (g) $III_{Zr}AA$; (h) $III_{Zr}AC$; (i) $III_{Zr}AB$; (j) III_BAA; (k) III_BAB (The big green spheres represent Zr atoms. The small grey spheres are for B; while the small brown spheres are the C atoms of graphene. The Zr/B atoms beneath the graphene layer are in red to highlight the different stacking structures of the top and bottom ZrB_2 slabs)

Figure 16: Variation of the interfacial energy (E_b, J/m^2) with the interlayer distance (d, Å).

Figure 17: Variation of the interfacial energy (E_b, J/m^2) with the in-plane strains (%) in (a) ZrB_2 matrix and (b) graphene fiber.

Figure 18: Variation of (a) the chemical bonding energy (E_b, J/m^2) and (b) the detachment stress (σ, GPa) with interlayer distance (d, Å); top projection of the interface type (c) I, (d) II and (e) III. (the large green spheres are for Zr atoms, while the small brown ones are for the C atoms in graphene.)

Figure 19: Variation of (a) the interface decohesion energy (ΔE_{cov}, J/m^2) and (b) the cleavage stress (σ, GPa) with the initial crack opening distance (Å).

Figure 20: Variation of (a) the sliding energy corrugation (ΔE, J/m^2) and (b) the shear stress (σ,GPa) for the interface shearing ways of s101: (0001)<$11\overline{2}0$> and s110: ($10\overline{1}0$) <$11\overline{2}0$>.

Table 1: Elastic constants, moduli and Possion ratio of MB_2 (M=Ti, Zr and Hf) as calculated with GGA-DFT using the two numerical implementation contained in the code VASP and AIMS and comparison with the experimental data.

List of Abbreviations and Symbols

UHTCMC	Ultra-High Temperature Ceramic Matrix Composite
UHTC	Ultra-High Temperature Ceramic
CMC	Ceramic Matrix Composite
SiC	Silicon Carbide
C	Carbon
DFT	Density Functional Theory
FE	Finite Element
MD	Molecular Dynamics
α	Thermal Expansion Coefficient
κ	Thermal Conductivity
G	Shear Modulus
E	Young’s Modulus
B	Bulk Modulus
ν	Poisson Ratio

1. Executive Summary

The ultra-high temperature ceramic matrix composites (UHTCMCs) developed in the C^{3}harme project are based on UHTC materials (such as ZrB_2, HfB_2, ZrC, HfC, TaC), infiltrated with carbon or SiC fibers. Although the various materials to be developed are structured at the meso- and macro-scale, they are characterized by the presence of a rich variety of interfaces, including phase interfaces, grain boundaries and surfaces. The interfaces are commonly the sites of damage initiation under thermal and mechanical loads [1], for example they can nucleate the softening and the melting of grain boundaries, the crack propagation along phase interfaces, etc. Therefore, the ultimate performances of UHTCMCs largely rely on the interfaces. In general the details of the interface properties are not easily experimentally accessible (in particular at high temperature), so that atomistic simulations are the only tools for characterization. In this deliverable we will present our understanding of interfaces obtained from the first principles (no free parameters) atomistic simulations.

In particular, we have calculated the materials-specific thermo-mechanical parameters of MB_2 (M=Ti/Zr/Hf) matrix materials. These provide useful information and can be further employed in the description of the composites within finite elements (FE) methods. Such properties include the thermal expansion, the thermal conductivity, the heat capacity, the elastic tensor, the temperature dependent bulk modulus, the ideal tensile and shear strength and the critical cleavage stress. Then, we have evaluated the stable surface morphology of matrix materials, to establish the most likely surface exposed to the bonding with the C fibers. This is crucial for establishing the atomic structures of matrix/fiber interfaces. Thereafter, we have constructed atomic models of phase interfaces between the matrices and the C fibers, and calculated the associated interfacial energies for various interface candidates. The interface strain and the chemical interaction were explored as well. These are helpful for understanding how the matrices and the C fibers bond together and what is their interface strength. Furthermore our study gives hints on possible design strategies to make either weak or strong interfaces. Lastly, we have examined the interface response to mechanical deformation in two fundamental modes: shearing events, where atoms switch neighbors, and crack nucleation events, in which atoms lose the net number of neighbors and form a crack (free surfaces) in the end. All these results build up a dataset, which will be used to construct and verify force fields for molecular dynamic simulations at elevated temperatures. This step is necessary to extend our simulation capabilities to the meso-scale at elevated temperatures.

All the calculations presented in this deliverable were performed at the level of density functional theory (DFT) [2], which allows one to calculate materials properties *ab initio*, namely without the need of experimental parameters. The VASP code [3] with the plane-wave basis projector augmented wave (PAW) [4] method was adopted. The generalized gradient approximation (GGA) with the parameterization of Perdew, Burke and Ernzerhof (PBE) [5] was used to describe the exchange and correlation potential, including van der Waals interactions by DFT-D2 correction [6].

2. Thermal properties of MB_2 matrices

For the thermo-mechanical properties, we focused on MB_2 (M= Zr and Hf) materials. These are very promising ultra-high temperature structural ceramics, because of the extremely high melting temperature (T_m>3000 °C), good thermal and electrical conductivities, excellent thermal shock resistance, and chemical inert to molten metals. ZrB_2 is currently the material of choice for the composites experimentally made in C^3harme. Here our analysis has been extended to TiB_2 and HfB_2 so that general trends can be extracted. In this section, the Young's modulus, the bulk modulus, the elastic tensor, the ideal strength and the cleavage behavior (for understanding the brittle fracture) will be calculated. Note that all those quantities are intrinsic material parameters, which can be obtained from single crystal calculations. They set up a reference basis for understanding the effects of interfaces, and provide the dataset for FE and MD simulations. At the same time our results are compared with available experimental reports, in order to validate the reliability of our parameters-free DFT method.

2.1 Thermal expansion

Thermal expansion is important for high temperature structural ceramic materials. The thermal stress will form if the structural parameters change significantly at high temperature. Thereby, the reliability of aerospace components will be also affected. In this subsection, we report the structural parameters of two of the most promising matrix materials, ZrB_2 and HfB_2, at high temperatures (T > 1150 K). Experimental data are available for ZrB_2 only, while for HfB_2 our predictions are ahead of experiments.

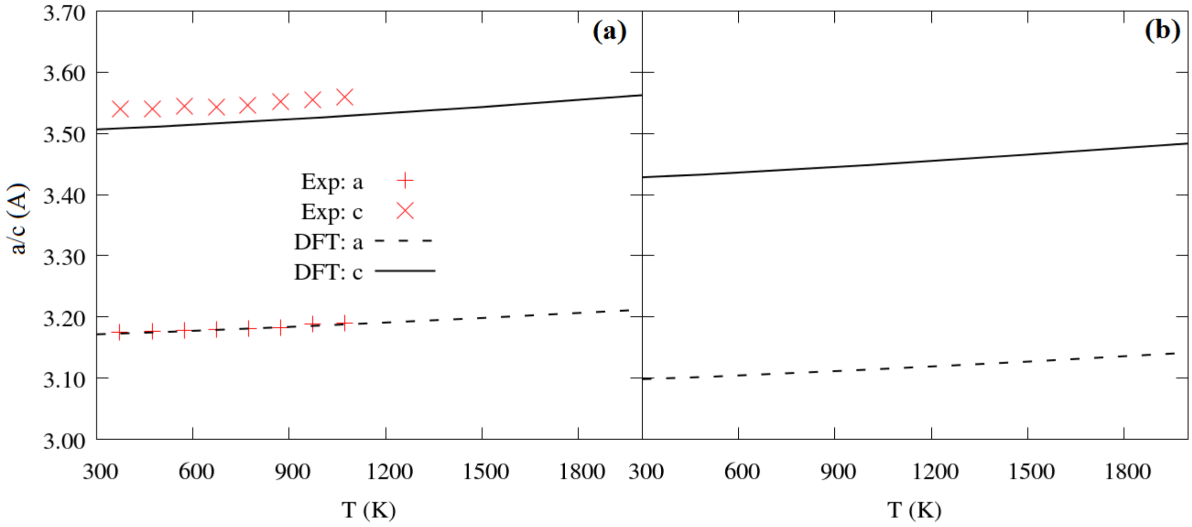

Figure 21: Temperature-dependent lattice constants (*a/c*, Å) of hexagonal (a) ZrB_2 and (b) HfB_2 obtained from DFT calculations and comparison with experimental data [7].

The thermal dependence of the *a* and *c* lattice parameters are presented in Figs. 1(a) and (b) for ZrB_2 and HfB_2, respectively. An experimental report exists for ZrB_2 below 1150 K [red stars and crosses in Fig. 1(a)]. Our DFT results agree very well with the measurements, with the *a* parameter being identical to what measured, while a 1% deviation is found for the *c* lattice constant. This indicates a good reliability of the DFT calculations. Furthermore, the DFT calculations also predict the high temperature structural parameters above 1200 K for both ZrB_2 and HfB_2. This is a range never explored and therefore missing in literature. Thus, these data are very useful for quantifying the thermal stress at high temperature, in particular they extend previous studies to the temperature range of interest for aerospace applications.

2.2 Thermal conductivity

Thermal conductivity plays a significant role in the thermal stress and the thermal shock resistance of high temperature structural ceramics. Since ZrB_2 and HfB_2 are good electrical conductors, their thermal conductivities comprise contributions from both electron and phonon transport. The former ($\boldsymbol{\kappa_{el}}$, $W \cdot m^{-1} \cdot K^{-1}$) could be calculated by using the Wiedemann-Franz law:

$$\kappa_{el} = L\sigma T \,, \qquad \textbf{(1)}$$

where, *L* is known as the Lorenz constant, 2.44×10^{-8} $W \cdot \Omega \cdot K^{-2}$. The electrical conductivity (σ) is adopted from experiments [9]. The contribution from phonon transport to the thermal conductivity ($\boldsymbol{\kappa_{ph}}$, $W \cdot m^{-1} \cdot K^{-1}$), or called the lattice thermal conductivity, is calculated by the Debye-Slack model:

$$\kappa_{ph} = A\frac{\bar{M}\Theta_a^3\delta n^{1/3}}{\gamma^2 T}\,. \qquad \textbf{(2)}$$

For calculation details of $\boldsymbol{\kappa_{ph}}$ we refer to Ref. [10], and finally the total thermal conductivity is derived as:

$$\kappa_{total} = \kappa_{el} + \kappa_{ph}\,. \qquad \textbf{(3)}$$

Our calculation results are shown in Fig. 2 (a) and (b) for ZrB_2 and HfB_2, respectively. The DFT results (red curves) have a reasonable agreement with experiments **[7, 8]**. For ZrB_2, the DFT results are compared with two sets of experiments. Note that the measurements are affected by the purity and the porosity of the samples, so they are not expected to map exactly on our DFT results, which are likely to provide an upper bound to the thermal conductivity. The measurements in Ref. [7] are for samples with higher densification and in fact our results agree better with them. In general, our DFT estimate gives us $\boldsymbol{\kappa_{el}}$ much larger than $\boldsymbol{\kappa_{ph}}$ for both ZrB_2 and HfB_2. This indicates that the good thermal conductivity of ZrB_2 and HfB_2 mainly originates from the electronic thermal conductivity.

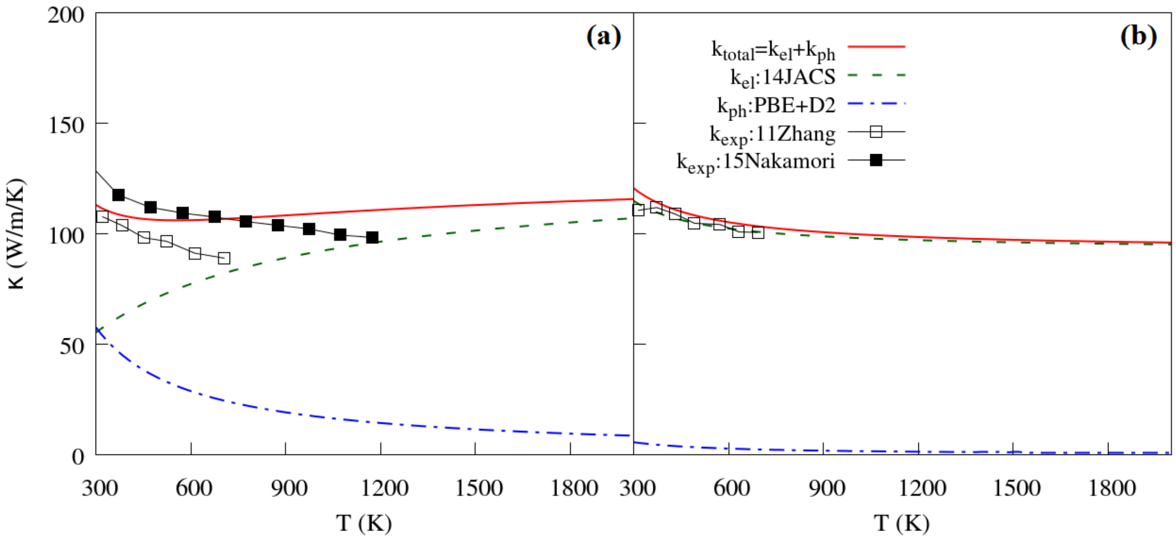

Figure 22: The thermal conductivity of (a) ZrB_2 and (b) HfB_2 predicted by DFT and a comparison with available experimental data [7, 8]. The dashed green and blue lines represent respectively the calculated electron and phonon contributions to the thermal conductivity, while the red line is the total. Note that most of the high-temperature thermal conductivity has to be attributed to the electronic component.

2.3 Heat capacity

The heat capacity at a constant volume can be obtained from:

$$C_V^{ph}(T) = k_B \int \frac{(\hbar w)^2 e^{\hbar w/k_B T}}{(k_B T)^2 (e^{\hbar w/k_B T} - 1)^2} \,, \qquad \mathbf{(4)}$$

where k_B is Boltzmann constant, ω denotes the phonon frequency, and $g(\omega)$ is phonon density of states (DOS). The total heat capacity at a constant pressure can be evaluated by:

$$C_P(T) = C_V^{ph}(T) + \alpha_V^2 BVT \,. \qquad \mathbf{(5)}$$

Here, α_V is the volume thermal expansion coefficient, B is the bulk modulus, while V is the cell volume. The calculation results are displayed in Figs. 3(a) and (b) again for ZrB_2 and HfB_2. Also in this case a good agreement with experimental data [7] is shown for ZrB_2, while no experimental data are available for HfB_2. Furthermore, our calculations extend the available data to a much higher temperature range.

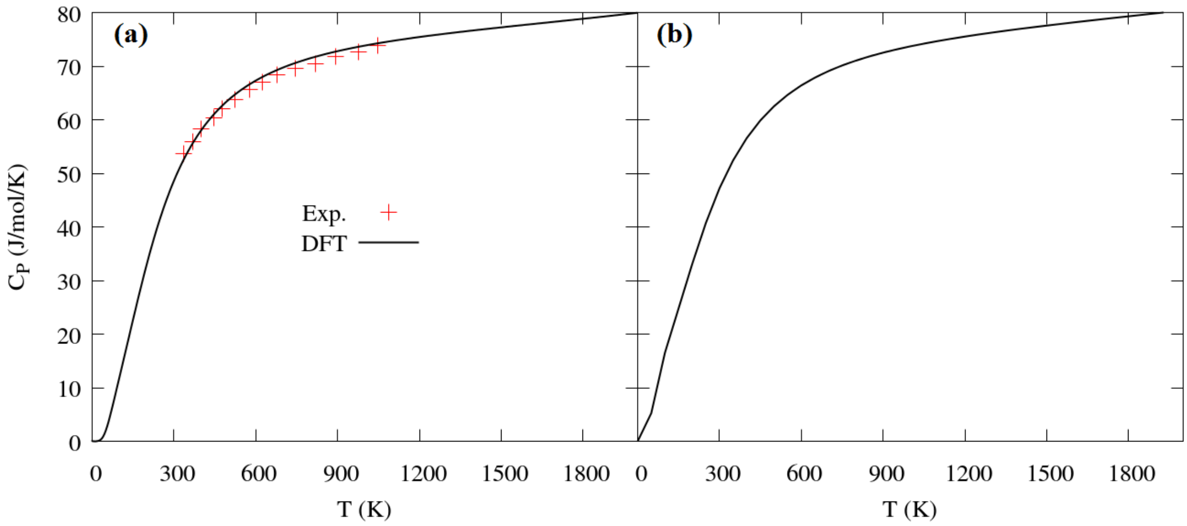

Figure 23: The heat capacity of (a) ZrB_2 and (b) HfB_2 predicted by DFT and a comparison with experimental data [7]. Data for HfB_2 are not available.

3. Mechanical properties of MB_2 matrices

3.1 Elasticity

The elasticity investigation provides important parameters necessary for micro/meso-scale modeling. Here the elasticity of MB_2 (M=Ti, Zr and Hf), including the elastic tensors of single crystals, bulk moduli, Young's moduli and Poisson' ratio of polycrystallines are calculated and summarized in Table 1. A good agreement with experimental data is achieved also for these set of properties.

Furthermore, the temperature dependence of bulk modulus is calculated. The results are displayed in Figs. 4(a) and (b) for ZrB_2 and HfB_2, respectively. Although there is a slight deviation from the measurements at medium temperature, our calculations still provide the missing high-temperature data.

Table 2: Elastic constants, moduli and Possion ratio of MB_2 (M=Ti, Zr and Hf) as calculated with GGA-DFT using the two numerical implementations contained in the codes VASP and AIMS and a comparison with experimental data when available.

	TiB_2			ZrB_2			HfB_2	
	Exp[11]	VASP	AIMS	Exp[11]	VASP	AIMS	VASP	AIMS
c_{11}	655	568	652	568	574	652	615	594
c_{12}	57	57	66	57	56	55	42	66
c_{13}	98	121	100	121	116	120	115	120
c_{33}	455	441	454	441	459	433	473	444
c_{44}	263	258	258	258	264	252	287	260
c_{66}	299	256	293	256	258	253	207	264
B	260	265	252	240	251	256	249	248
E	-	524	483	489	488	463	485	454
G	-	224	204	-	208	193	207	190
ν	-	0.170	0.181	-	0.176	0.199	0.175	0.196

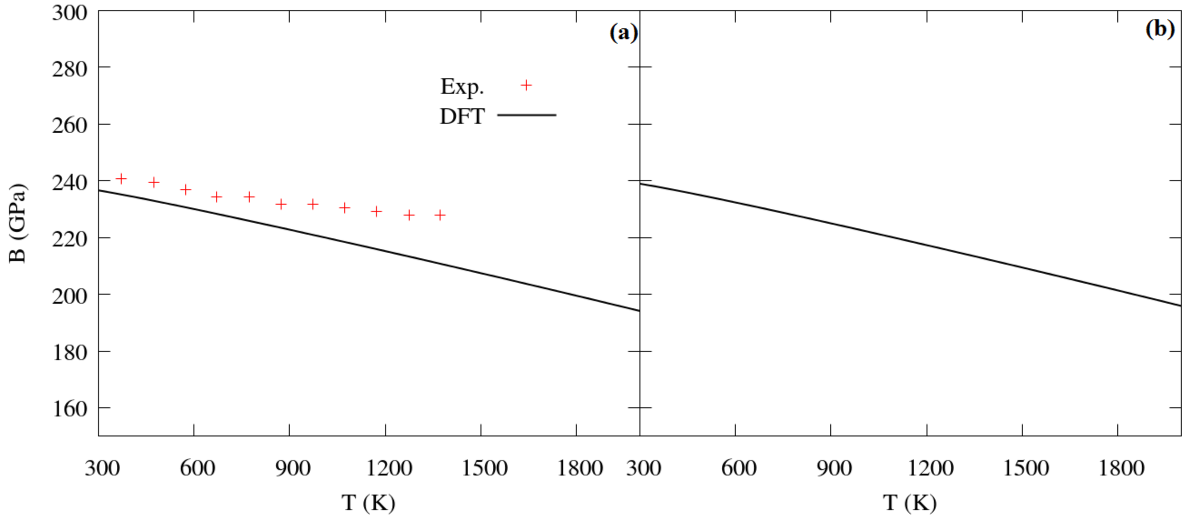

Figure 24: The DFT-predicted temperature dependence of the bulk moduli of (a) ZrB_2 and (b) HfB_2 and a comparison with experiments [12]. Our calculations extend the available temperature range for ZrB_2 and provide the full characterization for HfB_2.

3.2 Elastic anisotropy

MB_2 (M=Zr/Hf) materials have a nano-laminate hexagonal structure with the metal and the boron atoms alternatively stacking along the *c* direction. As such anisotropy of the properties along the *a* and *c* directions is expected and must be quantify. For instance, a strong elastic anisotropy will affect the way cracks propagate.

Here, we calculate the orientation dependence of the Young's and shear moduli for ZrB_2 and HfB_2. Figures 5 (a) and (b) show the 3D orientation dependence of the Young's moduli of ZrB_2 and HfB_2, respectively. They both have a drum-like shape, indicating slight anisotropy along the *c* direction. Besides, HfB_2 has a higher elastic anisotropy than ZrB_2. The projections of Young's moduli and Shear moduli onto the $(10\bar{1}0)$ plane are illustrated in Figs. 6 (a) and (b), separately. They further confirm the slightly elastic anisotropy at small strains.

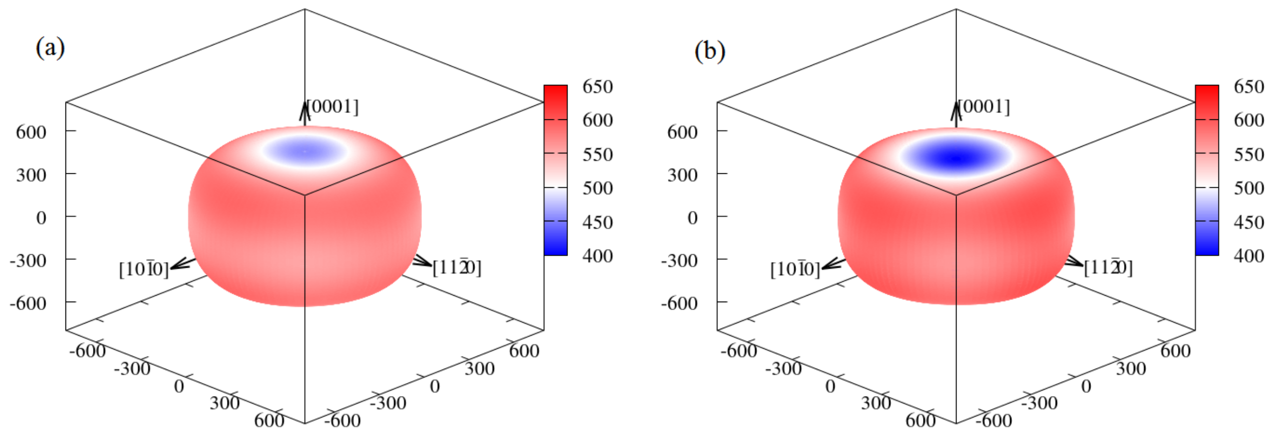

Figure 25: 3D orientation dependence of the Young's moduli of (a) ZrB_2 and (b) HfB_2 as predicted by DFT.

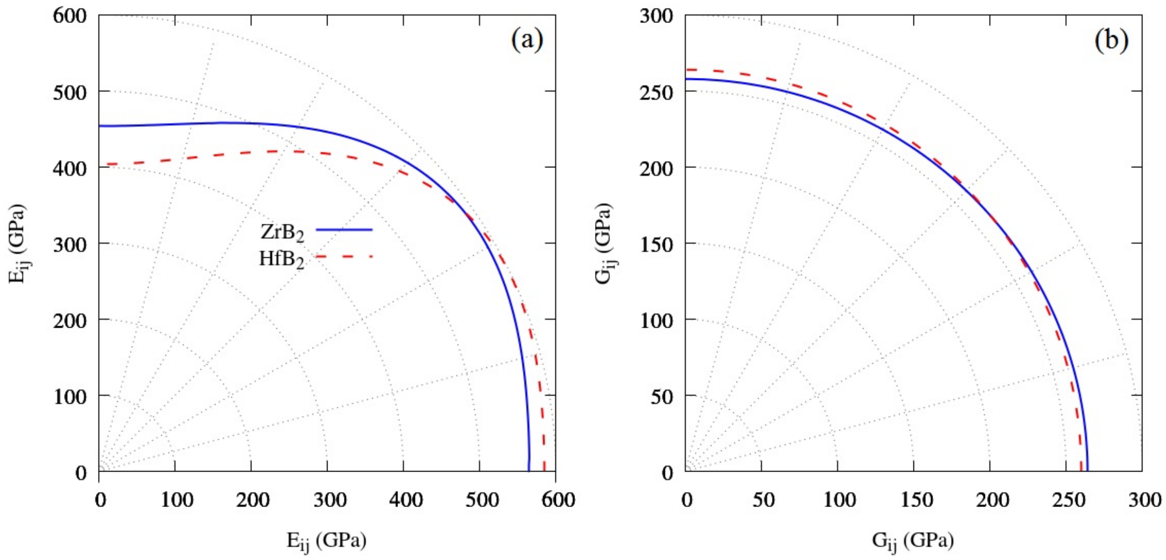

Figure 26: Projection of (a) the Young's moduli and (b) the Shear moduli onto the $(10\bar{1}0)$ plane.

3.3 Ideal strength

In addition to the elasticity, the mechanical responses at large strains are important to understand the failure mechanism of MB_2 materials. Hence, the strain-stress relationship was calculated to predict the ideal strength. Figures 7 and 8 show the results for ZrB_2 and HfB_2 under tensile and shear modes, respectively.

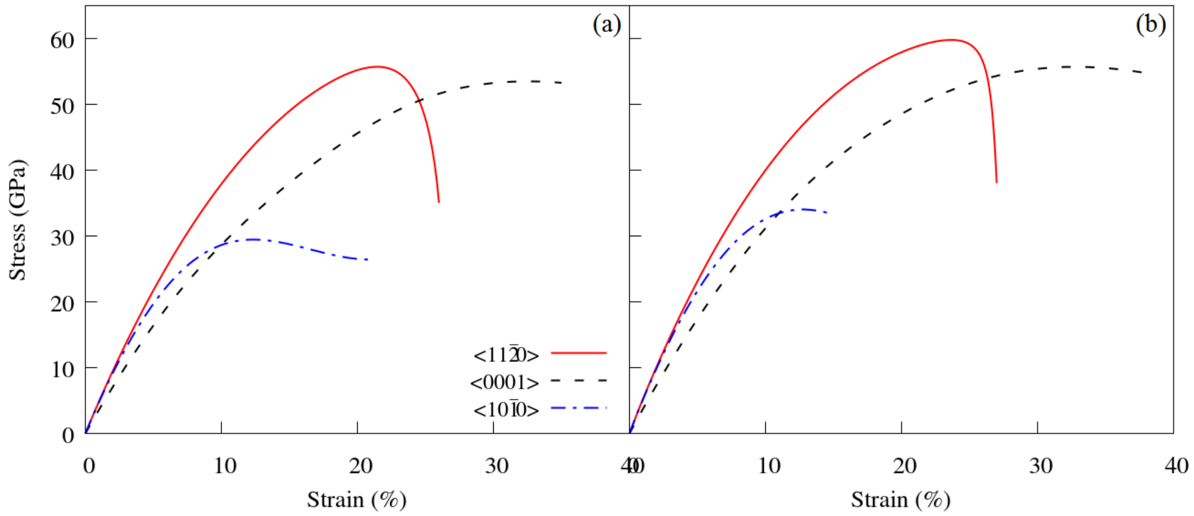

Figure 27: DFT-calculated stress-strain relationship for (a) ZrB_2 and (b) HfB_2 under tensile mode.

At variance with the small elasticity anisotropy at small strains, the tensile strength along [$\mathbf{10\bar{1}0}$] is almost two times lower than those along [$11\bar{2}0$] and [0001]. Also, the shear strength along ($\mathbf{10\bar{1}0}$)[$11\bar{2}0$] is 60% lower than the others. Those results indicate easy tension along [$\mathbf{10\bar{1}0}$] and easy shear along ($\mathbf{10\bar{1}0}$)[$11\bar{2}0$]. Therefore, when considering large strains, the ($\mathbf{10\bar{1}0}$) atomic plane becomes the most relevant for failures.

Note that all those mechanical properties were derived for single crystals. The effects of grain boundaries and defects were not included. Moreover, homogenous deformation was applied here. This corresponds to a slow loading mode, in which enough time is given to the materials to globally respond to the mechanical loads.

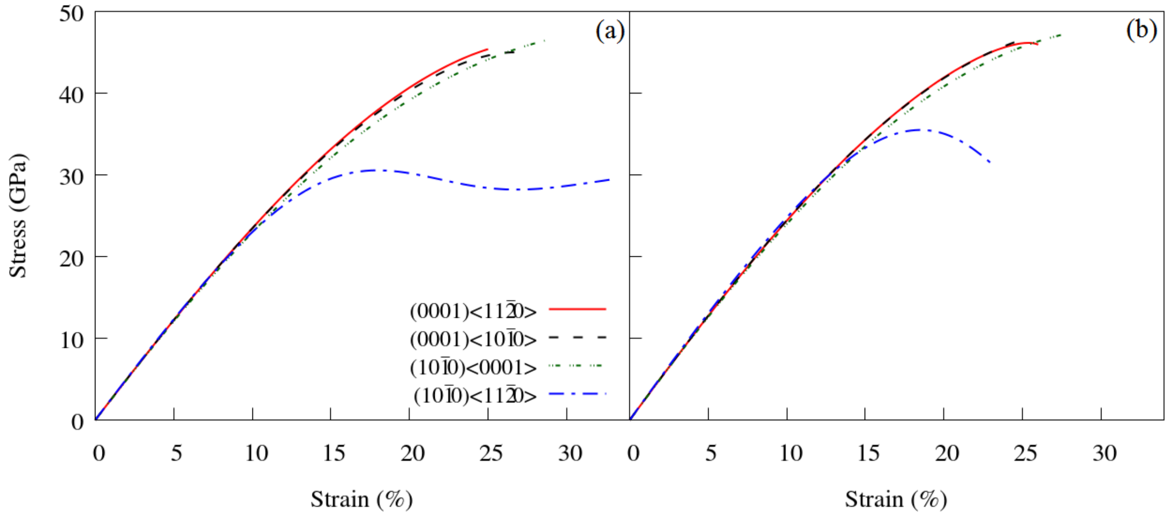

Figure 28: DFT-calculated stress-strain relationship for (a) ZrB_2 and (b) HfB_2 under shear mode.

3.4 Cleavage and brittle fracture

In order to understand the crack formation process in MB_2 materials, we have calculated the decohesion energy and the cleavage stress during the cleavage. At variance with the global deformation mode described in section 3.3, the localized deformation is applied by constraining the crack opening distance between specific atomic planes. The cleavage directions [0001], [10$\bar{1}$0], [10$\bar{1}$1], [11$\bar{2}$0], [11$\bar{2}$2] and [11$\bar{2}$3] were all considered in order to extract the global anisotropic cleavage behavior. Note we studied the brittle cleavage without structural relaxation here. This corresponds to the fast loading mode.

Our results are illustrated in Figs. 9(a-d). As shown in Figs. 9(a) and (b), when the cleavage opening distance is larger than 3 Å, the decohesion energy reaches a plateau for both ZrB_2 and HfB_2. This corresponds to the bond breaking and to the formation of a free surface (crack formed). Moreover, the critical cleavage stress goes in the range of (18,33) GPa. This is two times lower than that of the homogenous tensile mode. Therefore, the investigation of cleavage deformation should have a higher priority in order to understand the mechanical properties of UHTCs. Moreover, the critical cleavage stress corresponds to a critical crack opening distance around 0.51-0.68 Å.

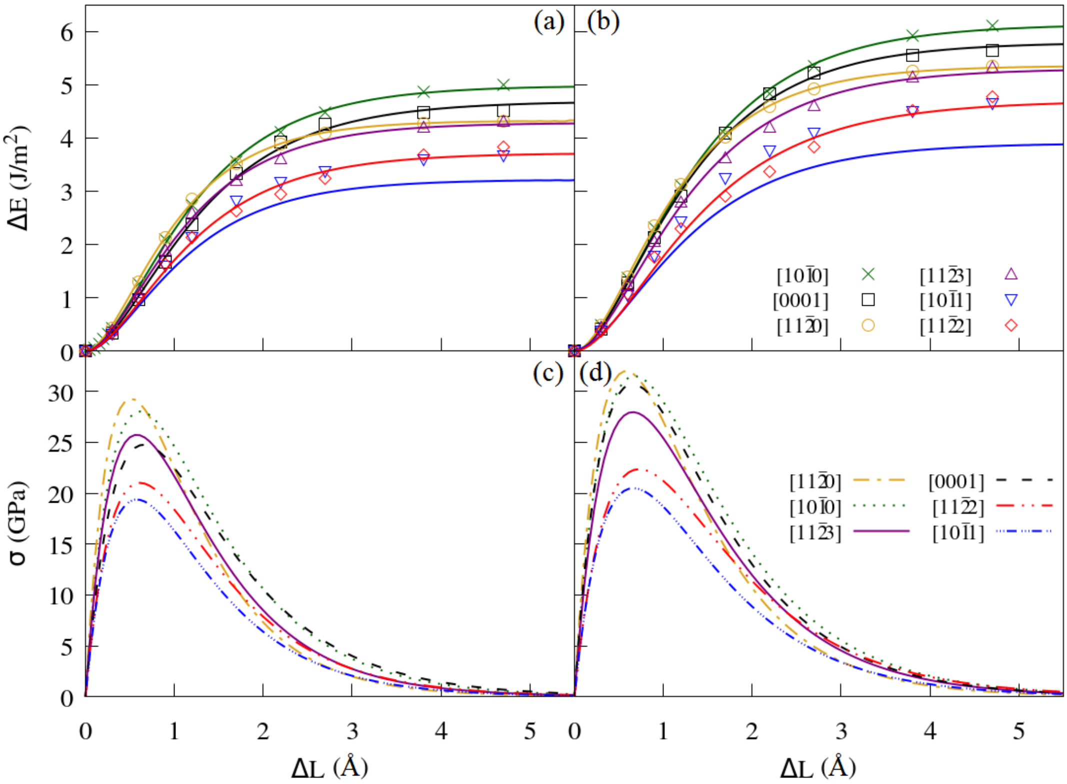

Figure 29: Variation of the decohesion energy (ΔE, J/m^2) in (a) ZrB_2 and (b) HfB_2 as a function of crack opening distance (ΔL, Å), and the corresponding cleavage stress (σ, GPa) in (c) ZrB_2 and (d) HfB_2.

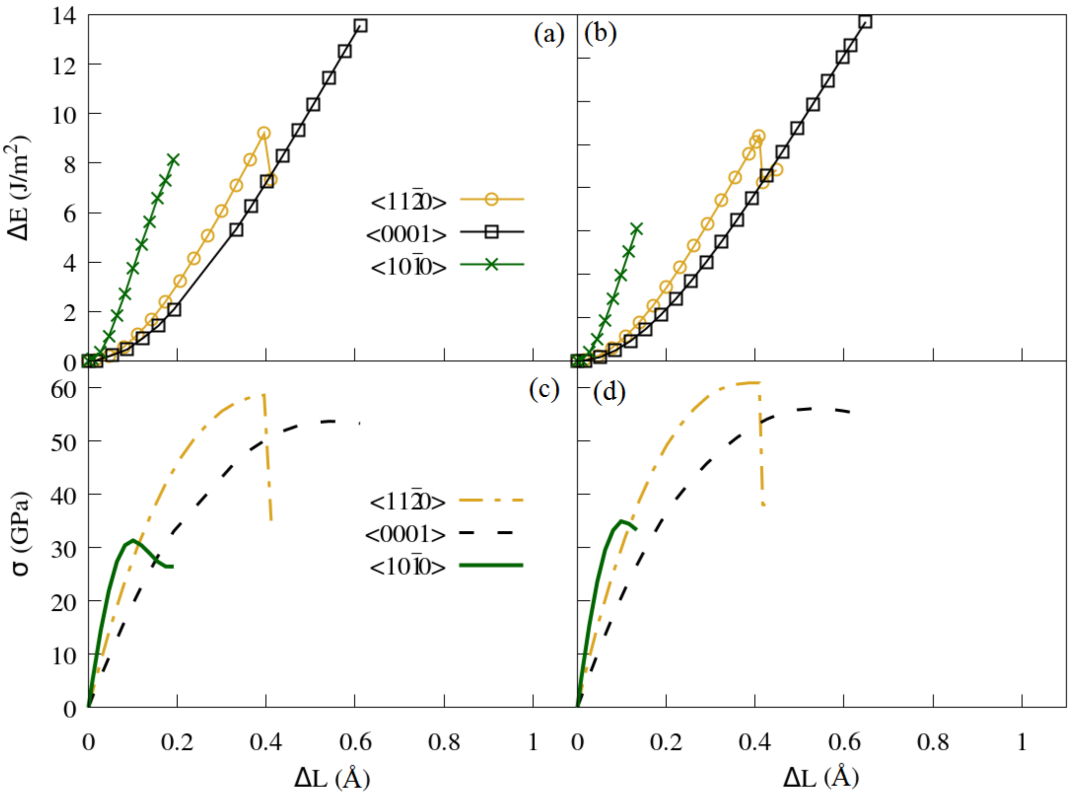

Figure 30: Variation of system energy in (a) ZrB_2 and (b) HfB_2 under homogenous tensile loads; and the stress-strain relationship with the variation of interlayer distance in (c) ZrB_2 and (d) HfB_2.

In order to further understand the cleavage deformation, we have compared it with the tensile deformation by re-plotting the latter on the scale of the interlayer distance. As shown in Figs. 10(a) and (b), the system energy shows a much steeper energy increase than that of the cleavage deformation. Moreover, the tensile deformation shows a more obvious anisotropy than that of the cleavage. In the tensile mode, the material has an intense global response to deformation. In contrast, the brittle cleavage deformation is locally constraint between two atomic planes and no in-plane relaxation is allowed in such a fast loading mode. This explains why the critical cleavage stress is lower than the ideal tensile strength.

4. Thermodynamics of surfaces

The investigation of surfaces aims at establishing the most likely surface exposed to the bonding with the C fibers. Thereby, some important parameters like the orientation and termination species of interface models should be established. In this way, more accurate micro-models of interfaces can be constructed, an asset particularly important when experimental parameters are not accessible.

4.1 Surface structures

The atomic structures of MB_2 (M=Ti/ZrHf) surfaces are built up by cleaving the bulk material along the basal, prismatic and pyramidal planes. The surface termination species of both M and B are considered. In the end, twelve candidate surface structures are selected, as illustrated in Figs. 11(a-l). The details of the surface construction and the testing of the surface slab thickness could found in our recent publication [13].

The cleavage plane and the termination species determine the notation for the surfaces. For example, $(0001)_M$ and $(0001)_B$ stand for the surfaces formed from [0001] cleavage with termination species of M and B, respectively. The $(10\bar{1}0)_{B(B)}$ and $(10\bar{1}0)_{B(M)}$ are surfaces obtained from the $[10\bar{1}0]$ cleavage with a B termination surface and a second layer of B and M atoms, respectively.

After selecting the potential surface candidates in MB_2 (M=Ti/Zr/Hf) matrices, the stable surface morphology was identified by evaluating their surface formation energies. This will be discussed in the following section.

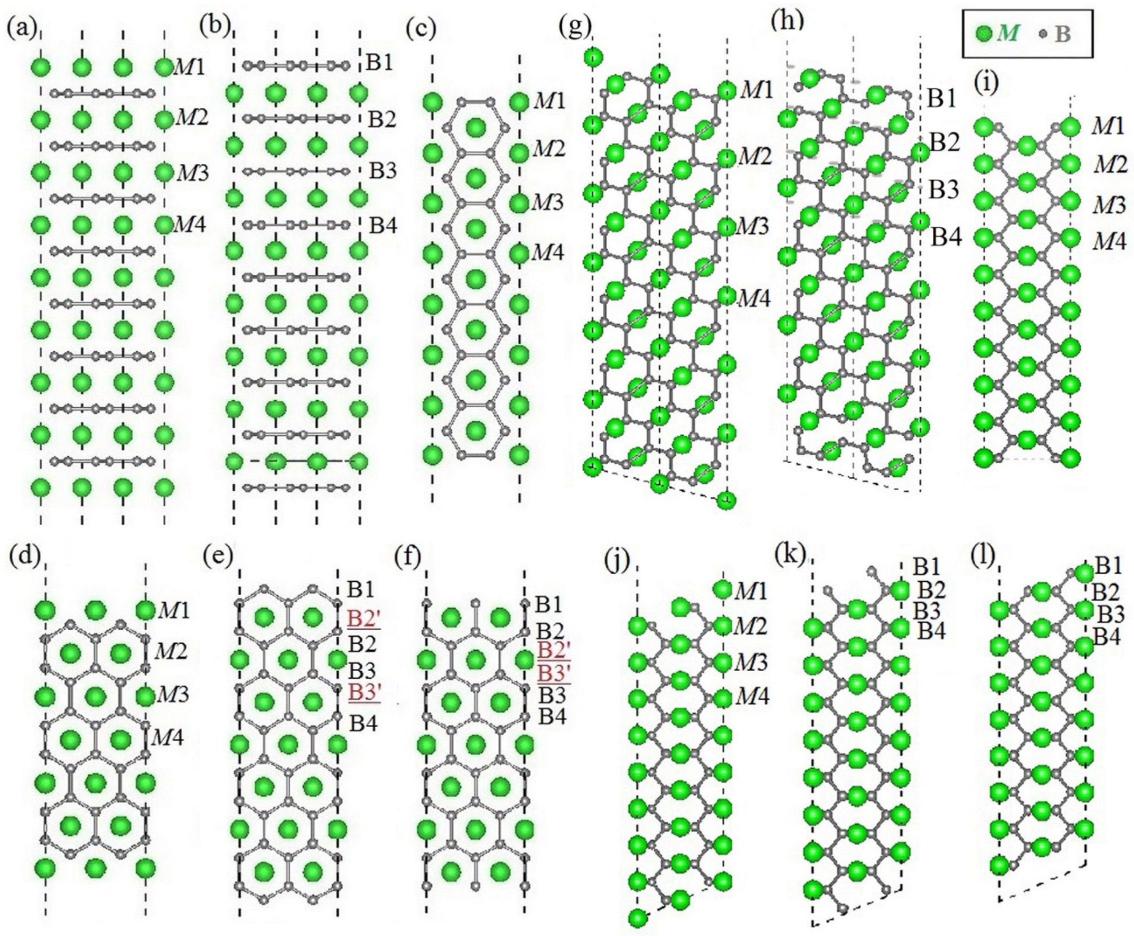

Figure 31: Various surface structures investigated: (a) $(0001)_M$; (b) $(0001)_B$; (c) $(11\bar{2}0)_{M+B}$; (d) $(10\bar{1}0)_M$; (e) $(10\bar{1}0)_{B(B)}$; (f) $(10\bar{1}0)_{B(M)}$; (g) $(11\bar{2}\bar{3})_M$; (h) $(11\bar{2}\bar{3})_B$; (i) $(11\bar{2}\bar{2})_{M+B}$; (j) $(10\bar{1}1)_M$; (k) $(10\bar{1}1)_B$ and (l) $(10\bar{1}1)_{B(M)}$. (The metal atoms are represented by the big green spheres; while the small grey spheres are the B atoms). For the surface notation please see the text.

4.2 Surface phase diagrams

The surface formation energies were calculated as a function of the chemical potential as:

$$\boldsymbol{\sigma = \frac{1}{2A}(E_{slab} - N_M\mu_M^{slab}} - N_B\mu_B^{slab}). \qquad \textbf{(6)}$$

Here, E_{slab} is the total energy of a fully relaxed surface slab, $\boldsymbol{\mu_M^{slab}}(\boldsymbol{\mu_B^{slab}})$ and $\boldsymbol{N_M}(\boldsymbol{N_B})$ are the chemical potential and the number of *M* (B) atoms in the surface slab, respectively, and *A* is the surface area.

Our results are shown in Figs. 12, 13 and 14 for TiB_2, ZrB_2 and HfB_2, respectively. At the end, five types of surfaces are established to be stable when going from a *M*-rich to a B-rich environment, respectively, $(0001)_M$, $(10\bar{1}0)_M$, $(10\bar{1}1)_{B(M)}$, $(11\bar{2}\bar{3})_M$ and $(0001)_B$. The highly stable $(10\bar{1}0)_M$, $(10\bar{1}1)_{B(M)}$ and $(11\bar{2}\bar{3})_M$ surfaces were identified here for the first time.

The mechanism behind the surface stability was analyzed in terms of cleavage energy, surface strain and surface bonding states. The details have been published in Ref. [13]. Those calculation results provide important information for a better understanding of the most likely surfaces exposed to the fibers in UHTCMCs.

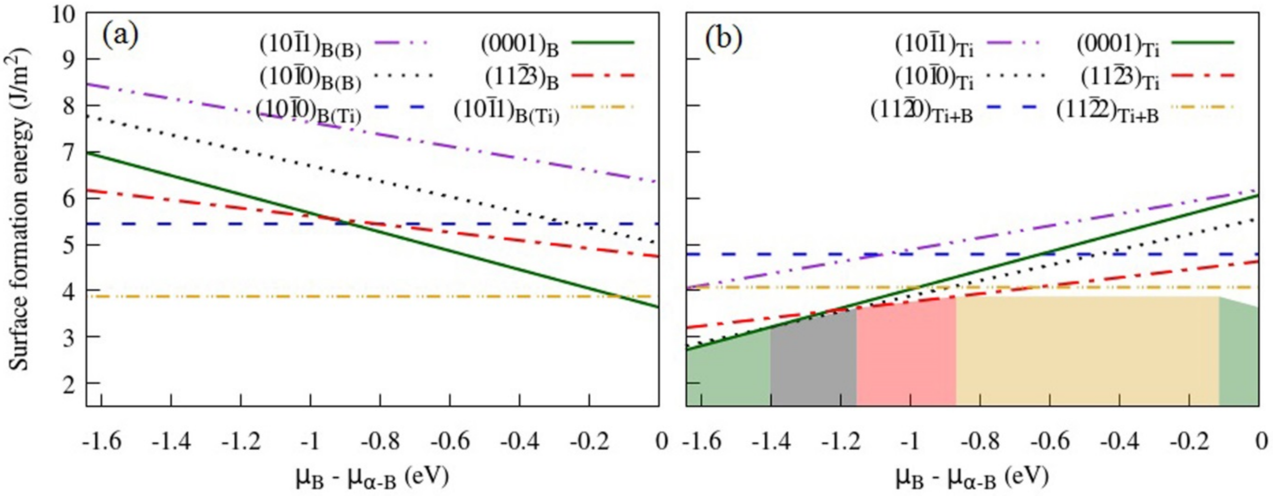

Figure 32: Surface formation energies of (a) B-terminated and (b) (Ti+B)- or Ti-terminated surfaces in TiB_2. The shaded areas mark the stable regions of $(0001)_{Ti}$, $(10\bar{1}0)_{Ti}$, $(11\bar{2}3)_{Ti}$, $(10\bar{1}1)_{B(Ti)}$, and $(0001)_B$ surfaces, when going from Ti-rich to B-rich conditions. The chemical potential of boron, $\Delta\mu_B = \mu_B^{slab} - E_B^{bulk}$ is taken with respect to that of bulk α-rhombohedral boron.

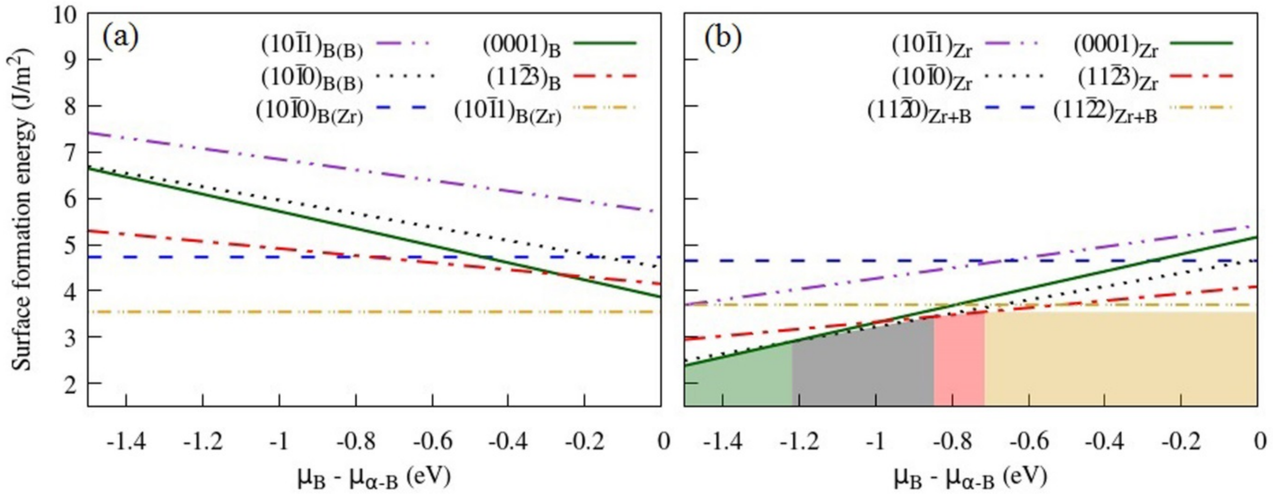

Figure 33: Surface formation energies of (a) B-terminated and (b) (Zr+B)- or Zr-terminated surfaces in ZrB_2. The shaded areas mark the stable regions of $(0001)_{Zr}$, $(10\bar{1}0)_{Zr}$, $(11\bar{2}3)_{Zr}$ and $(10\bar{1}1)_{B(Zr)}$ surfaces, when going from Zr-rich to B-rich conditions. The chemical potential of boron, $\Delta\mu_B = \mu_B^{slab} - E_B^{bulk}$ is taken with respect to that of bulk α-rhombohedral boron.

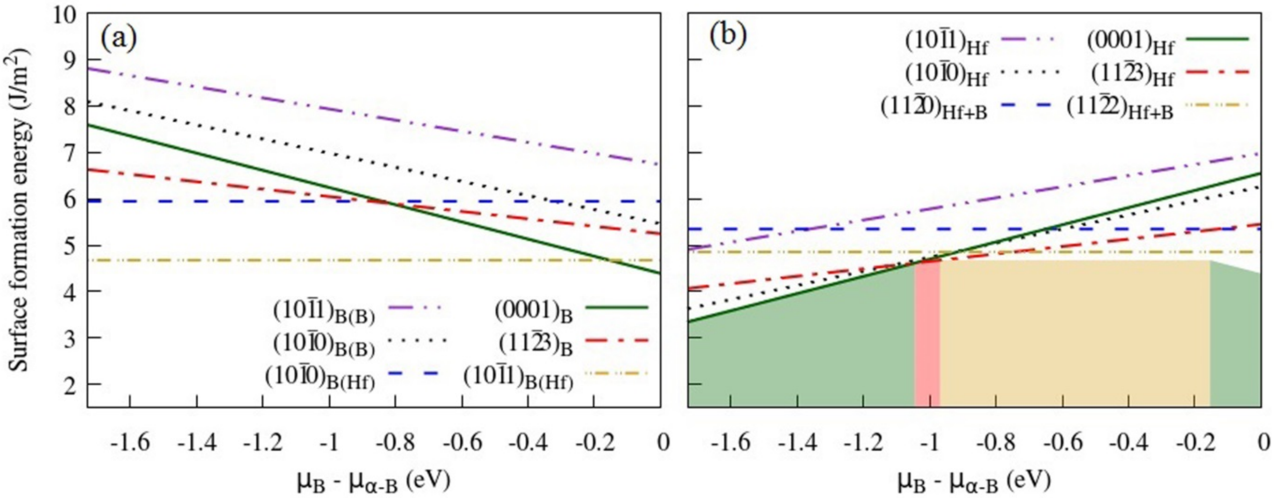

Figure 34: Surface formation energies of (a) B-terminated and (b) (Hf+B)- or Hf-terminated surfaces in HfB_2. The shaded areas mark the stable regions of $(0001)_{Hf}$, $(11\bar{2}3)_{Hf}$, $(10\bar{1}1)_{B(Hf)}$, and $(0001)_B$ surfaces, when going from Hf-rich to B-rich conditions. The chemical potential of boron, $\Delta\mu_B = \mu_B^{slab} - E_B^{bulk}$ is taken with respect to that of bulk α-rhombohedral boron.

5. Interfaces

In this section, the interfacial energies and the interface responses to mechanical loads will be discussed. These provide important information for the understanding of the interface behavior. Firstly, we build up the atomistic models of the interfaces in accordance with the stable surface morphology discussed previously. Secondly, the interface adhesion, interface stains and the interface chemical bonding were explored. Thirdly, the mechanical responses to two fundamental deformation modes: decohesion events, in which atoms lose the net number of neighbors (often irreversibly) and shearing events, where atoms switch neighbors, were investigated.

5.1 Interface structures

The interface model of UHTCMCs was constructed by the sandwich structure ZrB_2/Graphene/ZrB_2, where graphene provides a reliable proxy to the more complex C fiber used in experiments (note that a full description of the C fiber is outside the capabilities of our *ab initio* methods). The structural variables of the hybrid model, like the orientation and the termination species of ZrB_2 matrix, the stacking structure of the ZrB_2 slabs and graphene, the interlayer distance and in-plane lattice parameters, should be judiciously specified.

Following the idea that the stable surfaces are the most likely structures to be exposed to the C fibres, we set up the orientation and the termination species of ZrB_2 slabs, i.e. the $(0001)_{Zr/B}$ and $(10\bar{1}0)_{Zr/B}$ surface slabs. In order to consider the effects of interface strains, it is meaningful to have supercell slabs with different in-plane sizes. In short, the interface models were built up based on three types of ZrB_2 supercell slabs, namely I: $\sqrt{3}a\times\sqrt{3}a$ (0001); II: $2a\times3c$ $(10\bar{1}0)$; III: $2a\times2a$ (0001). A balls and sticks diagram of these structures is presented in Fig. 15.

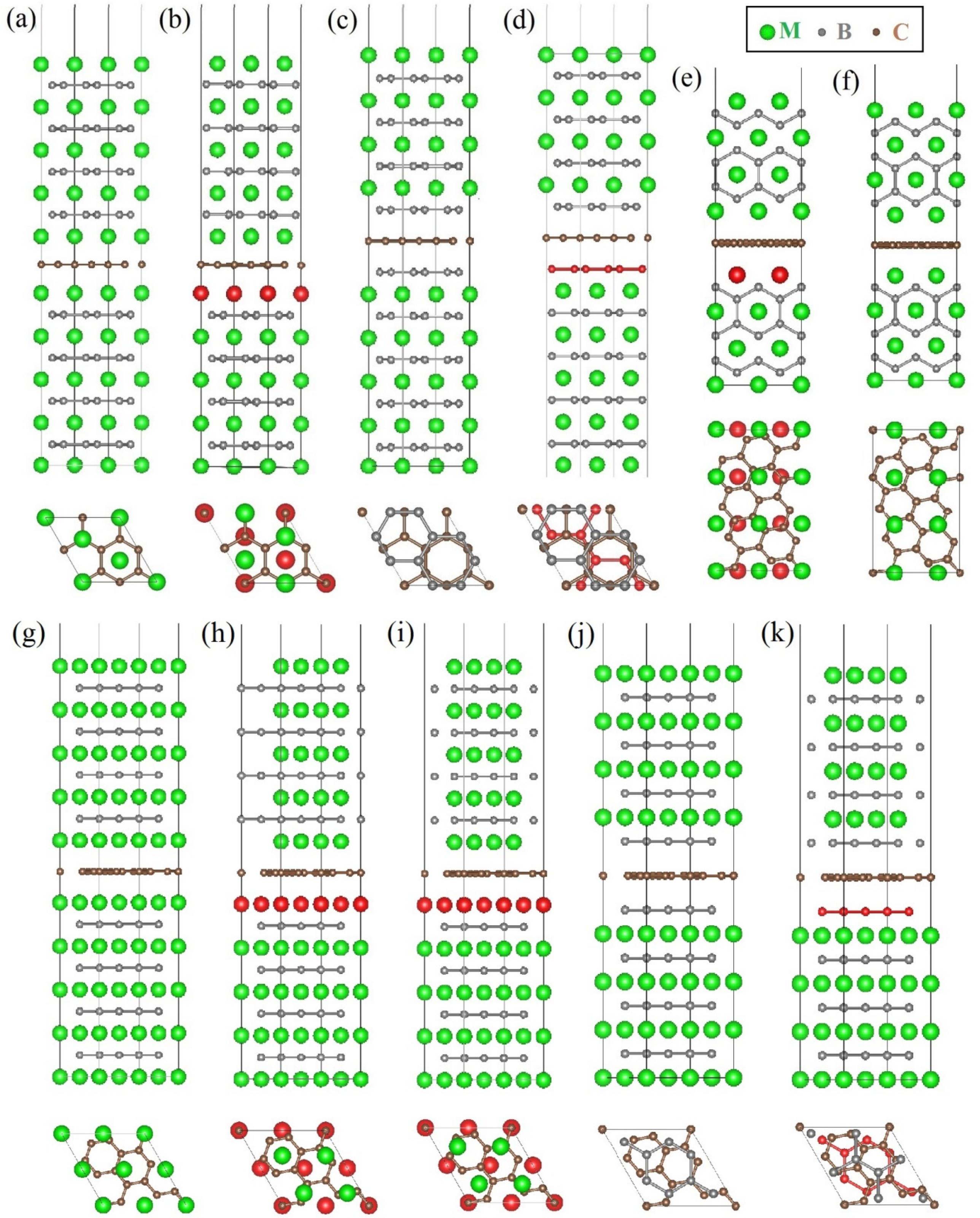

Figure 35: Front and top view of heterostructures of (a) $I_{Zr}AA$; (b) $I_{Zr}AB$; (c) I_BAA; (d) I_BAB; (e) $II_{Zr}AA$; (f) $II_{Zr}AB$; (g) $III_{Zr}AA$; (h) $III_{Zr}AC$; (i) $III_{Zr}AB$; (j) III_BAA; (k) III_BAB (the large green spheres represent Zr atoms, the small grey spheres are for B atoms, while the small brown spheres are the C atoms in graphene. The Zr/B atoms beneath the graphene layer are in red to highlight different stacking ways of top and bottom ZrB_2 slabs)

The coupling of the ZrB_2 slab and graphene was obtained using the coincidence lattice method, in which the rotation and the straining of graphene and ZrB_2 slab were tune to ensure a low interface mismatch. In the end, eleven hetero-structures were constructed, as illustrated in Figs. 15 (a-f). The notation of various hybrid structures follow the setup of ZrB_2 slabs (I/II/III), the stacking ways of ZrB_2 slab (AA/AB/AC) and the termination species of ZrB_2 slab (Zr/B). The top and bottom ZrB_2 slabs were stacked in ways of either AA, AB or AC:

AA: the Zr atoms of the top ZrB_2 slab locate on the atop sites of the Zr atoms in the bottom ZrB_2 slab;

AB: the Zr atoms of the top ZrB_2 slab sit on the bridge sites of the Zr atoms in the bottom ZrB_2 slab;

AC: the Zr atoms of the top ZrB_2 slab reside on the hollow/center sites of underlying Zr atoms in the bottom ZrB_2 slab.

5.2 Interface adhesion

The interface adhesion could be characterized by studying the rigid separation of the matrix and the fibers, and the strength of the interface adhesion could be measured by calculating the interfacial energy. This was defined as the energy released per unit area when forming a hybrid structure from two isolated surface slabs:

$$E_b = \frac{E(a_i) - E^{top}(a_0) - E^{bottom}(a_0) - E^G(l_{C-C})}{2A} \,. \qquad \textbf{(7)}$$

Here, A is the interface area. $\boldsymbol{E(a_i)}$, $\boldsymbol{E^{top}(a_0)}$, $\boldsymbol{E^{bottom}(a_0)}$ and $\boldsymbol{E^G(l_{C-C})}$ are respectively the total energies of the hybrid structure, the top ZrB_2 slab, the bottom ZrB_2 slab and the graphene slab. Note that the in-plane lattice parameter of ZrB_2 slab is from the bulk a_0; while the in-plane lattice constant of graphene is determined from the C-C bond length of $l_{C\text{-}C}$=2.40 Å. In this way, the reference states are strain-free for various types of hybrid structures (I/II/III). We did not choose the equilibrium bulk structures as reference, since in that case surface effects would be ignored.

Our results for the interfacial energies are illustrated as a function of the interlayer distance in Fig. 16, and as a function of the in-plane strain in Fig. 17. The lower is E_b, the stronger is the interface adhesion. That is to say, the E_b curve with a deeper energy indicates a more stable interface.

Moreover, the interfacial energy of the various interface types asymptotically converges to different values, as illustrated in Fig.16. The interface types I_{Zr} and I_B all converge to U_1 regardless of the stacking ways; while that of type II and III go to U_2 and U_3, respectively. This indicates that interfaces are in different strain states. Note that the interface adhesion characterized by the interfacial energy is the result of a syngeneic effect of the interface strain and the interface chemical bonding.

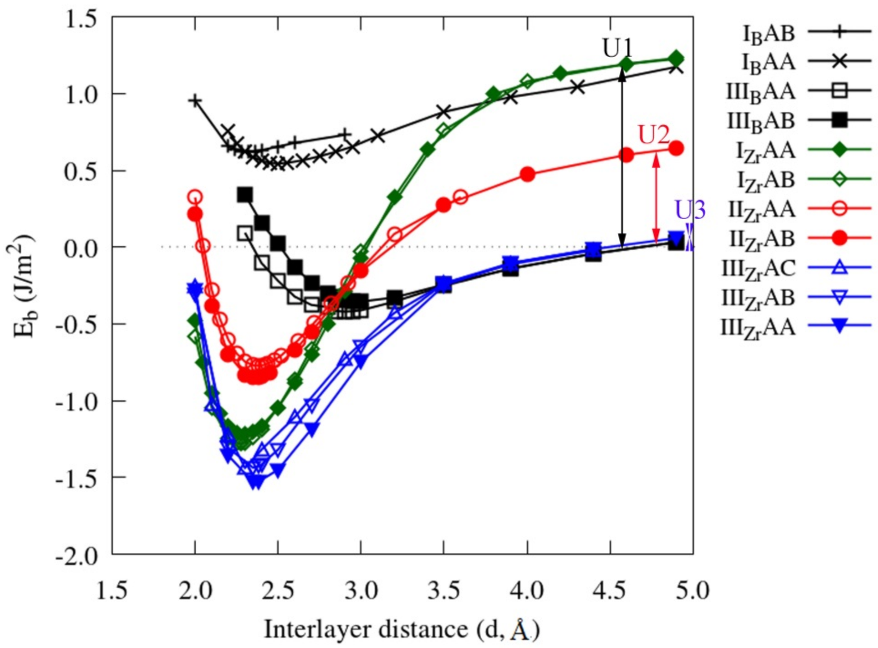

Figure 36: Variation of the interfacial energy (E_b, J/m^2) with the interlayer distance (d, Å).

5.3 Interface strains

In the above section, we have mentioned that the various interface types are in a different strain states. From an atomistic view, the strain states in ZrB_2 slabs and C fibres are set by the common in-plane lattice parameters of the hybrid structures. For the three types of ZrB_2 slabs (I/II/III), we have calculated the interfacial energy change (E_b) with the strains in ZrB_2 matrix and graphene. Here, the in-plane strain of the ZrB_2 matrix and graphene are measured as:

$$\Delta_{ZrB_2} = \left(\frac{a_i}{a_{ZrB_2}} - 1\right) \times 100\% \,. \tag{8}$$

$$\text{and } \Delta_G = \left(\frac{a_i}{a_G} - 1\right) \times 100\% \,. \tag{9}$$

The results are presented in Fig. 17. A parabolic-like relation is noted for the change of interfacial energy with the in-plane strain. Since the in-plane strain could be adjusted by changing the content of the fibres, it is, in principle, possible to tune the interface adhesion. Interestingly, the in-plane strain of type I hybrid structures could be as large as 10%. As well-known a Moire pattern appears whenever the mismatch of graphene with a substrate approaches 5%-10%. Therefore, our modeling suggests that corrugation of the graphene sheet has to be expected in case of type I hybrid structures.

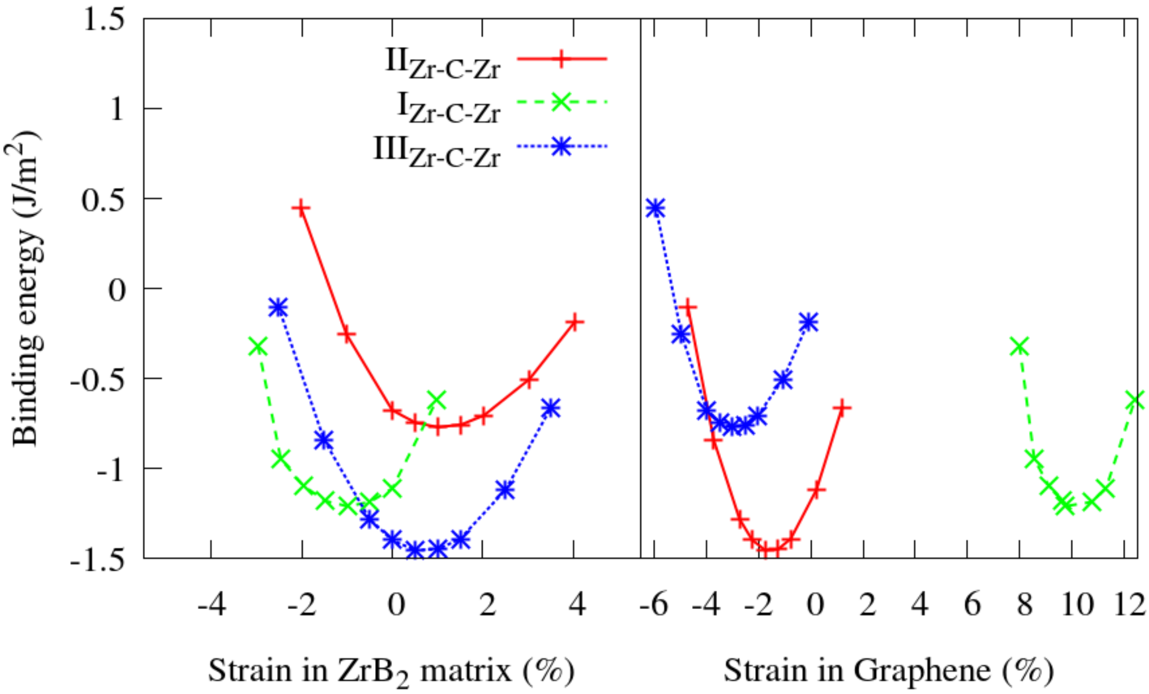

Figure 37: Variation of the interfacial energy (E_b, J/m^2) with the in-plane strains (%) in (a) ZrB_2 matrix and (b) graphene fiber.

5.4 Interface bonding

Since the interfacial energy follows a parabolic law with respect to strain, the strain effect and the chemical bonding effect could be decoupled. Here, we have removed the strain energy in the interfacial energy, E_b, through a modified Morse fitting:

$$E_b^{total}(d) = E_0 \times (\exp\big(-2a'(d-d_0)\big) - 2\exp\big(-a'(d-d_0)\big) + U \ . \quad \mathbf{(10)}$$

In this way, the chemical bonding at interfaces is described by Morse potential as:

$$E_b^{chemical}(d) = E_0 \times (\exp\big(-2a'(d-d_0)\big) - 2\exp\big(-a'(d-d_0)\big) \ . \quad \mathbf{(11)}$$

Here, d and d_0 are the interlayer distance and the equilibrium interface separation distance, respectively. U stands for the interface strain energy, E_0 represents the depth of the Morse potential well, showing how much energy is needed to detach the matrix from the fibre. The parameter $\boldsymbol{a'}$ correlates to the width of the Morse potential well.

The results of the chemical bonding energy ($\boldsymbol{E_b^{chemical}(d)}$) and the detachment stress (σ) of interfaces are illustrated in Figs. 18 (a-b). As shown, the interface bonding states could be categorized in three groups:

(i) Strong interface bonding: the interface I with Zr-C bonding has a deep E_0 well and high detachment stress (σ), which indicates a strong chemical interaction character. In Fig. 18(c), high bonding density of interface I could be identified;

(ii) Medium interface bonding: the interfaces II and III with Zr-C facing have a medium chemical bonding interaction. Those interfaces have a low bonding density as shown in Fig. 18(d-e). At the same time they have low interface strain.

(iii) Weak interface bonding: interfaces with B-C bonding show a shallow E_0 well and a low detachment stress (σ), suggesting weak interface bonding.

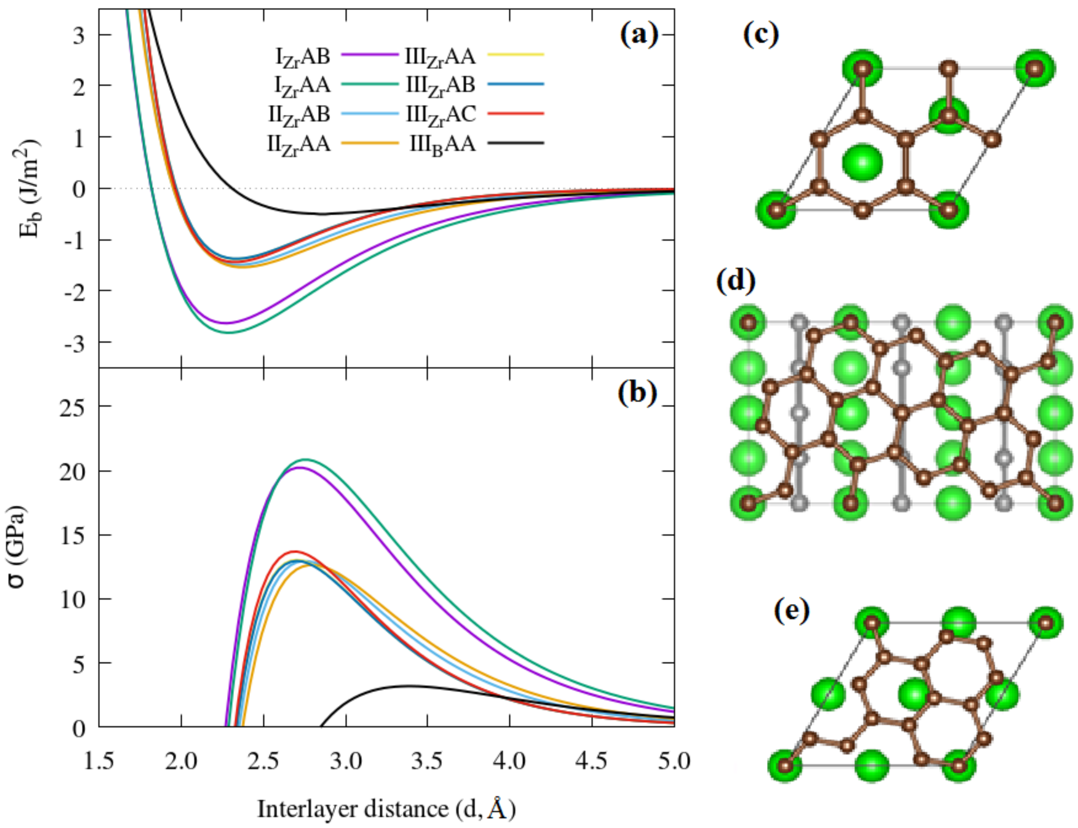

Figure 38: Variation of (a) the chemical bonding energy (E_b, J/m^2) and (b) the detachment stress (σ, GPa) with interlayer distance (d, Å); top projection of interface type (c) I, (d) II and (e) III (the big green spheres are for Zr atoms, while the small brown ones are for the C atoms in graphene.)

5.5 Interface crack

The responses of an interface to applied loads include interface sliding, interface decohesion, interface migration coupled to shear deformation, dislocation emission, crack nucleation and propagation. At the atomistic level, we have focused on two deformation modes: the interface shearing and the crack nucleation.

Four types of typical interface models are chosen for the investigation of crack nucleation, namely the hybrid-structures $I_{Zr}AB$, $III_{Zr}AA$ and $III_{B}AA$ for the crack along [0001] direction, and the hetero-structure $II_{Zr}AB$ for the crack along [10$\bar{1}$0] crystal orientation. An initial crack opening distance ranging from 0.0 to 3.5 Å were studied under single side cleavage loading.

The interface decohesion energy and the corresponding cleavage stress were calculated and are presented in Figs. 19(a) and (b). The cases of $I_{Zr}AB$ and $II_{Zr}AB$ have higher decohesion energies than that of $III_{Zr}AA$. This is not the same trend as that observed for the interfacial energy, but directly correlated with the chemical bonding energy. The same is also true for the cleavage stress. This is reasonable considring the crack initiated by breaking the interfacial Zr-C or B-C bonds. Therefore, the interface crack nucleation is strongly affected by the interface bonding strength. Other factors like interface defects or impurities will affect the crack nucleation by changing the interface bonding strength.

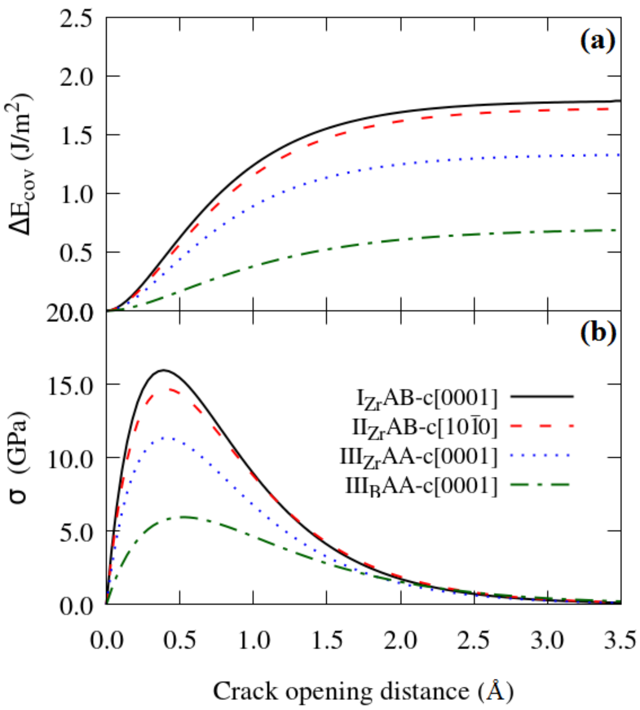

Figure 39: Variation of (a) interface decohesion energy (ΔE_{cov}, J/m^2) and (b) cleavage stress (σ, GPa) with initial crack opening distance (Å).

5.6 Interface sliding

The interface sliding modes of s101: (0001)<11$\bar{2}$0> and s110: (10$\bar{1}$0) <11$\bar{2}$0> were studied using the hybrid-structures $I_{Zr}AA$, $II_{Zr}AA$ and I_BAA. The results for the sliding energy corrugation and shear stresses are displayed in Figs. 20 (a) and (b), respectively. The sliding energy corrugation goes up from when considering $II_{Zr}AA$, $I_{Zr}AA$ and lastly I_BAA. The same trend was found for the corresponding shear stress. Note that these are much lower in magnitude than the interface decohesion energy and the cleavage stress, indicating that it is easier for the interface atoms to switch neighbors (sliding) than to lose neighbors to form cracks (breaking).

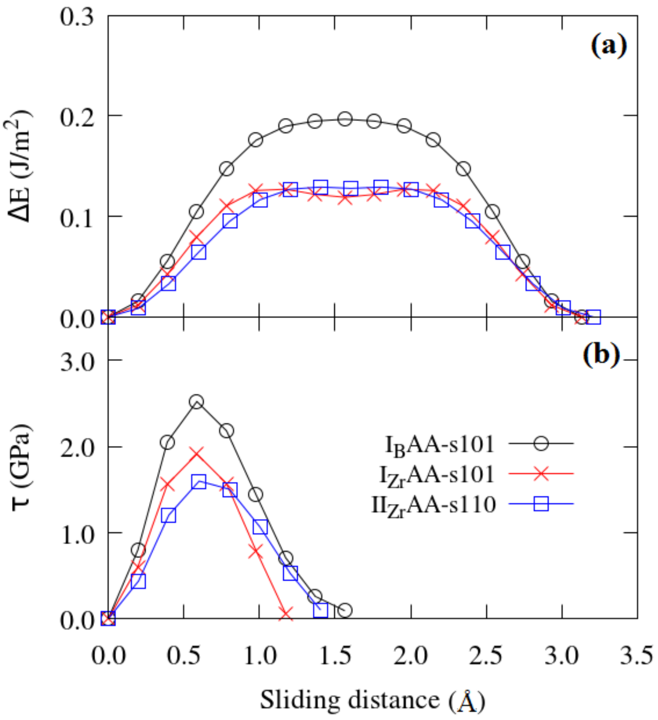

Figure 40: Variation of (a) sliding energy corrugation (ΔE, J/m^2) and (b) shear stress (σ,GPa) for interface shearing ways of s101: (0001)<11$\bar{2}$0> and s110: (10$\bar{1}$0) <11$\bar{2}$0>.

Note that our deformation investigation is limited by the in-plane lattice size, which in turn determines the cost of the atomistic simulation. As such, more complex and less commensurate structures (lower internal stress) cannot be studied with our methods. We are now working on the construction of a suitable force field to push up the simulation scales so that more structural details can be included. At the same time this will be helpful to the understanding of the temperature dependent properties of UHTCMCs, especially at high temperatures.

6. Conclusion and outlook

In this deliverable, we have presented the atomistic modeling of UHTCMCs at the DFT level. In particular:

(1) The thermo-mechanical properties of the $M\mathrm{B}_2$ (M=Ti/Zr/Hf) matrix materials are calculated, including thermal expansion, thermal conductivity, heat capacity, elasticity, ideal tensile, shear strength and crack nucleation. The calculation of these quantities is important, since they act as reference for the interface properties. At the same time, these data provide the input for microscale simulations using FE methods, and the testing dataset for force fields. These latter will allow one to perform high-temperature simulations using MD methods. Our calculation results are compared with experiments whenever available, which validates the reliability of our calculations. At the same time they extend the temperature range beyond what has been measured to date.

(2) The interface behavior is investigated by calculating the surface phase diagram, the interfacial energies, the interface strains and the interface bonding energies, together with the modeling of interface processes during cracks formation and the interfaces sliding. These offer important parameters not available from experiments. These data are helpful for understanding how the different materials are bonded together in UHTCMCs and how such bonding is modified by the design of atomic structures and compositions. Our results suggest that the damage mechanism of UHTCMCs can be somewhat tuned through a careful interface engineering.

Further studies including additional structural details like grain boundaries, dislocations and composition variation are important for understanding the complicated deformation behavior of UHTCMCs at the microscale. In addition, temperature dependent interface properties, such as creep, the melting and the reactivity of interfaces, waits for further exploration in the future. All those investigations would require a larger scale simulation, such as molecular dynamics and coarse-grained analysis. For this purpose, constructing a suitable force field for MD simulations would be our first next step.

References

[1] Y. Mishin, M. Asta, and J. Li, "Atomistic modeling of interfaces and their impact on microstructure and properties," *Acta Materialia,* vol. 58, pp. 1117-1151, 2010/02/01/ 2010.

[2] R. G. Parr and Y. Weitao, *Density-Functional Theory of Atoms and Molecules*: Oxford University Press, 1989.

[3] G. Kresse and D. Joubert, "From ultrasoft pseudopotentials to the projector augmented-wave method," *Physical Review B,* vol. 59, pp. 1758-1775, 1999.

[4] P. E. Blöchl, "Projector augmented-wave method," *Physical Review B,* vol. 50, pp. 17953-17979, 1994.

[5] J. P. Perdew, K. Burke, and M. Ernzerhof, "Generalized Gradient Approximation Made Simple," *Physical Review Letters,* vol. 77, pp. 3865-3868, 10/28/ 1996.

[6] G. Stefan, "Semiempirical GGA‐type density functional constructed with a long‐range dispersion correction," *Journal of Computational Chemistry,* vol. 27, pp. 1787-1799, 2006.

[7] F. Nakamori, Y. Ohishi, H. Muta, K. Kurosaki, K.-i. Fukumoto, and S. Yamanaka, "Mechanical and thermal properties of bulk ZrB2," *Journal of Nuclear Materials,* vol. 467, pp. 612-617, 2015/12/01/ 2015.

[8] L. Silvestroni and D. Sciti, "Densification of ZrB2–TaSi2 and HfB2–TaSi2 Ultra‐High‐Temperature Ceramic Composites," *Journal of the American Ceramic Society,* vol. 94, pp. 1920-1930, 2011.

[9] Y. Lei, Y. Jian, Q. Tai, Z. Jingxian, and P. Limei, "Microstructure, Mechanical, and Thermal Properties of (ZrB2 + ZrC)/Zr3[Al(Si)]4C6 Composite," *Journal of the American Ceramic Society,* vol. 97, pp. 2950-2956, 2014.

[10] Y. Zhang, B. Liu, J. Wang, and J. Wang, "Theoretical investigations of the effects of ordered carbon vacancies in ZrC1−x on phase stability and thermo-mechanical properties," *Acta Materialia,* vol. 111, pp. 232-241, 2016/06/01/ 2016.

[11] R. Kumar, M. C. Mishra, B. K. Sharma, V. Sharma, J. E. Lowther, V. Vyas*, et al.*, "Electronic structure and elastic properties of TiB2 and ZrB2," *Computational Materials Science,* vol. 61, pp. 150-157, 2012/08/01/ 2012.

[12] N. L. Okamoto, M. Kusakari, K. Tanaka, H. Inui, and S. Otani, "Anisotropic elastic constants and thermal expansivities in monocrystal CrB2, TiB2, and ZrB2," *Acta Materialia,* vol. 58, pp. 76-84, 2010/01/01/ 2010.

[13] Z. Yanhui and S. Stefano, "First‐principles investigation of the thermodynamic stability of MB2 materials surfaces (M = Ti/Zr/Hf)," *Journal of the American Ceramic Society,* doi:10.1111/jace.15547.